Large-Scale Computational Modeling of [Rh(DuPHOS)]$^+$-Catalyzed Hydrogenation of Prochiral Enamides: Reaction Pathways and the Origin of Enantioselection

Steven Feldgus and Clark R. Landis*

Contribution from the Department of Chemistry, University of Wisconsin−Madison, 1101 University Avenue, Madison, Wisconsin 53706

Received June 1, 2000

Abstract: The potential energy surface for the [Rh((*R*,*R*)-Me-DuPHOS)]$^+$-catalyzed asymmetric hydrogenation of a prochiral enamide, α-formamidoacrylonitrile, has been computed using a three-layer hybrid quantum mechanics/molecular mechanics method (ONIOM). The bond-breaking and bond-forming region is modeled using a nonlocal density functional method (B3LYP), whereas HF theory and molecular mechanics (UFF) are used to describe the electronic and steric impact of the outer coordination sphere of the catalyst. Intermediates and transition states were calculated along four isomeric pathways of two diastereomeric manifolds. The starting point for each manifold is a square planar catalyst−enamide complex. Binding of the *re* enantioface of the enamide to the catalyst generates the more stable, major diastereomer, favored by 3.6 kcal/mol over the minor diastereomer, which has the *si* face bound. However, the net free energy barrier for the reaction is 4.4 kcal/mol *lower* for the minor diastereomer than for the major diastereomer, making the minor diastereomer considerably more reactive and reproducing the "anti-lock-and-key" behavior observed experimentally in rhodium-catalyzed asymmetric hydrogenations. The difference in transition-state energies corresponds to an enantiomeric excess of 99.9% (*R*), within the range of experimental enantioselectivities of [Rh((*R*,*R*)-Me-DuPHOS)]$^+$ hydrogenations. The stability and reactivity differences of the two diastereomers are explained using simple steric and electronic arguments. The sequence of elementary steps, as well as the relative orderings of intermediates and transition states, is very similar to that found in our previous work on the achiral model system [Rh(PH$_3$)$_2$(α-formamidoacrylonitrile)]$^+$. We find oxidative addition to be the turnover-limiting step of the catalytic cycle. Our results are consistent with available empirical data for rhodium-catalyzed asymmetric hydrogenations, although more detailed experimental studies are needed on the specific model system studied herein.

I. Introduction

Highly selective catalysts are revolutionizing asymmetric synthesis. The invention of enantiospecific, Rh-based catalysts for the homogeneous hydrogenation of prochiral enamides in the early 1970s initiated intense efforts toward the discovery of new, more effective catalysts and the elucidation of the reaction mechanism.[1−8] New diphosphine ligands, such as DuPHOS[9−11] and PENNPHOS,[12−14] have led to catalysts that exhibit enzyme-like activities and selectivities for a wide variety of substrates. Commercial applications of catalytic asymmetric hydrogenation, such as the syntheses of L-DOPA,[15] candoxatril,[16] and Metolachlor,[17] illustrate the practical significance of modern asymmetric catalysts.

Detailed mechanistic studies of the [Rh(DIPAMP)]$^+$-catalyzed hydrogenation of acetamidocinnamates performed by Brown and co-workers[18−21] and by Halpern and co-workers[4,5,22−25] revealed the underlying sequence of steps by which [Rh(chiral diphosphine)]$^+$ catalysts transform enamides into chiral amino acid derivatives. Although the proposed sequence of reaction

(1) Ojima, I. *Catalytic Asymmetric Synthesis*; VCH: New York, 1993.
(2) Bosnich, B. In *Encyclopedia of Inorganic Chemistry*; King, R. B., Ed.; John Wiley & Sons: Chichester, 1994; Vol. 1, pp 219−236.
(3) Knowles, W. S. *Acc. Chem. Res.* **1983**, *16*, 106−112.
(4) Halpern, J. *Science* **1982**, *217*, 401−407.
(5) Halpern, J. In *Asymmetric Synthesis*; Morrison, J. D., Ed.; Academic: Orlando, FL, 1985; Vol. 5, pp 41−69.
(6) Koenig, K. E. In *Asymmetric Synthesis*; Morrison, J. D., Ed.; Academic: Orlando, FL, 1985; Vol. 5, pp 71−101.
(7) Noyori, R.; Takaya, H. *Acc. Chem. Res.* **1990**, *23*, 345−350.
(8) Stinson, S. C., *Chem. Eng. News* **1999**, *77* (41), 101−120.
(9) Burk, M. J. *J. Am. Chem. Soc.* **1991**, *113*, 8518−8519.
(10) Burk, M. J.; Feaster, J. E.; Nugent, W. A.; Harlow, R. L. *J. Am. Chem. Soc.* **1993**, *115*, 10125−10138.
(11) Burk, M. J. *Chemtracts−Org. Chem.* **1998**, *11*, 787−802.
(12) Jiang, Q.; Jiang, Y.; Xiao, D.; Cao, P.; Zhang, X. *Angew. Chem., Int. Ed.* **1998**, *37*, 1100−1103.
(13) Jiang, Q.; Xiao, D.; Cao, P.; Zhang, X. *Angew. Chem., Int. Ed.* **1999**, *38*, 516−518.
(14) Zhang, Z.; Zhu, G.; Jiang, Q.; Xiao, D.; Zhang, X. *J. Org. Chem.* **1999**, *64*, 1774−1775.
(15) Knowles, W. S. *J. Chem. Educ.* **1986**, *63*, 222−225.
(16) Burk, M. J.; Bienewald, F.; Challenger, S.; Derrick, A.; Ramsden, J. A. *J. Org. Chem.* **1999**, *64*, 3290−3298.
(17) Blaser, H.-U.; Spindler, F. *Chimia* **1997**, *51*, 297−299.
(18) Brown, J. M.; Chaloner, P. A. *Tetrahedron Lett.* **1978**, *21*, 1877−1880.
(19) Brown, J. M.; Chaloner, P. A. *J. Chem. Soc., Chem. Commun.* **1980**, 344−346.
(20) Brown, J. M.; Parker, D. *Organometallics* **1982**, *1*, 950−956.
(21) Brown, J. M.; Canning, L. R.; Downs, A. J.; Forster, A. M. *J. Organomet. Chem.* **1983**, *255*, 103−111.
(22) Chan, A. S. C.; Pluth, J. J.; Halpern, J. *Inorg. Chim. Acta* **1979**, *37*, L477.
(23) Chan, A. S. C.; Pluth, J. J.; Halpern, J. *J. Am. Chem. Soc.* **1980**, *102*, 5952−5954.
(24) Chan, A. S. C.; Halpern, J. *J. Am. Chem. Soc.* **1980**, *102*, 838−840.
(25) Landis, C.; Halpern, J. *J. Am. Chem. Soc.* **1987**, *109*, 1746−1754.

10.1021/ja0019373 CCC: $19.00
Published on Web 12/27/2000

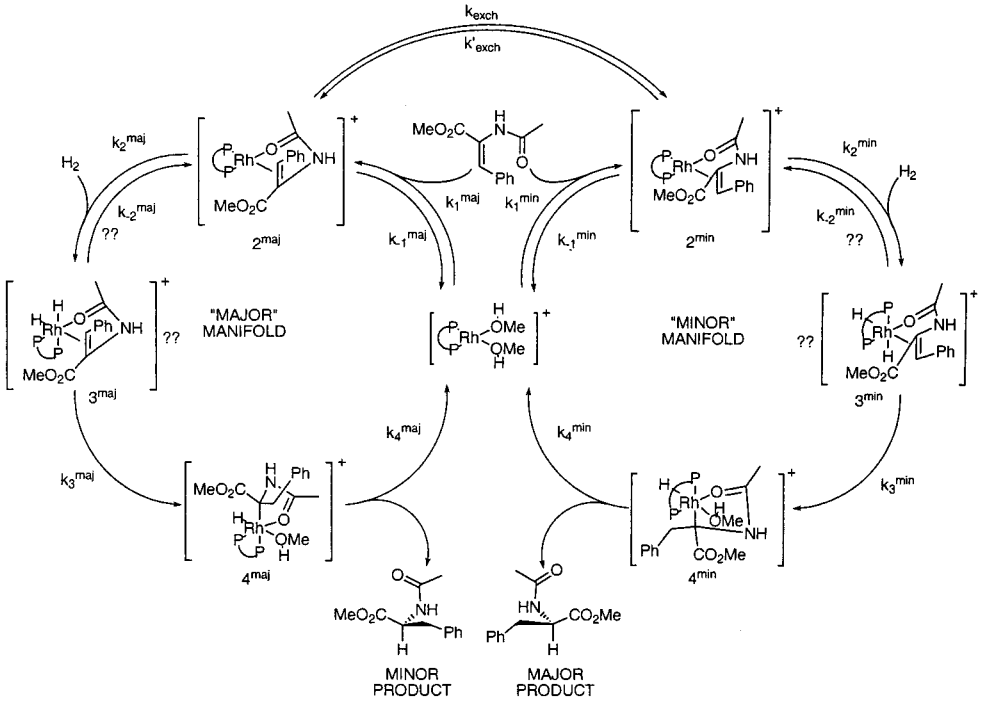

Figure 1. General mechanistic scheme for asymmetric hydrogenation. Question marks indicate uncharacterized steps and intermediates.

steps (binding of alkene followed by oxidative addition of hydrogen, then proceeding to product via migratory insertion and reductive elimination) is well precedented, these studies revealed a surprising "anti-lock-and-key" motif. Whereas the majority of the catalyst binds to one particular alkene enantioface, hydrogenation of the opposite enantioface leads to the hydrogenated product.

Advances in computing power and techniques in the past decade have made it possible to study large chemical systems at increasingly high levels of theory. Ten years ago, computational investigations of asymmetric hydrogenation catalysts were limited to molecular mechanics (MM) investigations. Two early MM investigations by Brown and Evans[26] and Bosnich et al.[27] suggested a common steric model for the origin of enantioselection in enamide hydrogenation, but a subsequent study from this laboratory using a more sophisticated MM method cast doubt on that steric model.[28] Two recent developments make the computations reported in this paper possible: the demonstration that hybrid density functionals efficiently model the quantum mechanics (QM) of organotransition metal complexes[29] and the rise of easily implemented QM/MM hybrid methods.[30]

Recently, we reported density functional theory (DFT) results for the hydrogenation of a small model substrate (α-formamidoacrylonitrile) with an achiral catalyst, $[Rh(PH_3)_2]^+$.[31] In that work, we verified that computations reproduce the structures and sequence of intermediates determined from experiment, identified molecular H_2 complexes and metal dihydrides as intermediates in the catalytic cycle, discovered the critical role played by the kinetics of molecular hydrogen complex formation

Scheme 1

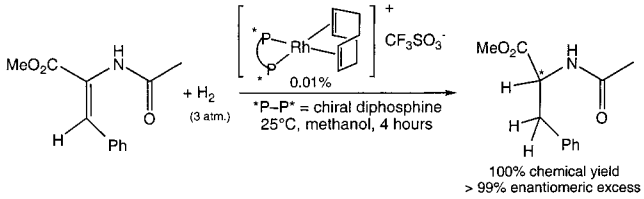

on the reaction pathways, and described a model for understanding the unusual H_2, HD, and D_2 kinetic isotope effects. However, this work falls short as a model for asymmetric catalysis because it is achiral and PH_3 is an unrealistic ligand model. In this paper, we report the full characterization of the catalytic cycle for the $[Rh(DuPHOS)]^+$-catalyzed hydrogenation of α-formamidoacrylonitrile using a three-layer ONIOM[32] model.

II. Background

A generic enantiospecific dehydroamino acid hydrogenation is shown in Scheme 1. Commonly the Rh catalysts are ligated by a chiral diaryl phosphine ligand (DIPAMP,[33] CHIRAPHOS,[34] BINAP,[7] etc.) or a bis(cyclophosphine) ligand (DuPHOS,[9−11] PENNPHOS[12−14]). The reaction conditions are mild: common temperatures are between 0 and 50 °C, hydrogen pressures span 0−100 atm, and a variety of solvents may be used (most commonly methanol). In general, the bis(cyclophosphine) ligated catalysts are faster, more selective, and more versatile than catalysts ligated by aryl phosphine ligands. Figure 1 illustrates the overall mechanism as determined for the $[Rh(DIPAMP)]^+$-catalyzed hydrogenation of methyl α-acetamidocinnamate.[19,23] The catalytic cycle consists of two coupled diastereomeric manifolds, with the majority of the catalyst (>90%) accumulating in the major manifold as **2^{maj}**. However, it is the reaction

(26) Brown, J. M.; Evans, P. L. *Tetrahedron* **1988**, *44*, 4905−4916.
(27) Bogdan, P. L.; Irwin, J. J.; Bosnich, B. *Organometallics* **1989**, *8*, 1450−1453.
(28) Giovanetti, J. S.; Kelly, C. M.; Landis, C. R. *J. Am. Chem. Soc.* **1993**, *115*, 4040−4057.
(29) Koch, W.; Hertwig, R. H. In *Encyclopedia of Computational Chemistry*; Schleyer, P. v. R., Ed.; John Wiley & Sons: Chichester, 1998; Vol. 2, pp 689−700.
(30) Maseras, F. In *Topics in Organometallic Chemistry*; Brown, J. M., Hofmann, P., Eds.; Springer-Verlag: Berlin, 1999; Vol. 4, pp 165−191.
(31) Landis, C. R.; Hilfenhaus, P.; Feldgus, S. *J. Am. Chem. Soc.* **1999**, *121*, 8741−8754.
(32) Svensson, M.; Humbel, S.; Froese, R. D. J.; Matsubara, T.; Sieber, S.; Morokuma, K. *J. Phys. Chem.* **1996**, *100*, 19357−19363.
(33) Vineyard, B. D.; Knowles, W. S.; Sabacky, M. J.; Bachman, G. L.; Weinkauff, D. J. *J. Am. Chem. Soc.* **1977**, *99*, 5946−5952.
(34) Fryzuk, M. D.; Bosnich, B. *J. Am. Chem. Soc.* **1977**, *99*, 6262−6267.

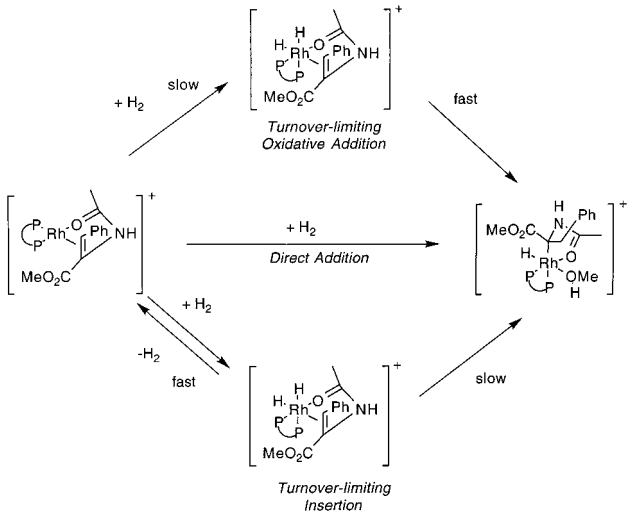

Figure 2. Three kinetic schemes that are consistent with the empirical rate data.

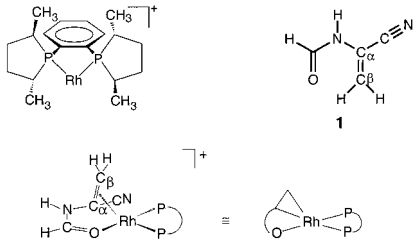

Figure 3. Catalyst and substrate (**1**) used in this study, and our cartoon representation of the initial catalyst−substrate complex.

of $\mathbf{2}^{\mathbf{min}}$ that accounts for the vast majority of hydrogenated product; i.e., catalysis follows an anti-lock-and-key motif. Spectroscopic studies by Brown, Burk, and Armstrong have established a similar reactivity pattern for diastereomers of [Ir(DuPHOS)(methyl α-acetamidocinnamate)]$^+$.[35]

Kinetic and spectroscopic studies by Landis and Halpern demonstrated that H_2 is involved in both the turnover-limiting and enantiodetermining step of the [Rh(DIPAMP)]$^+$-catalyzed enantioselective hydrogenation of dehydroamino acids.[25] The overall reaction rate is first-order in H_2 concentration (at least at low H_2 concentrations). At least three mechanistic pathways (Figure 2) are consistent with the existing data:[36] (1) enantiodetermining and turnover-liming oxidative addition of H_2 to the enamide−catalyst adduct, yielding a dihydride intermediate; (2) direct addition of H_2 to the enamide−catalyst adduct to form a metal alkyl hydride in a concerted fashion; and (3) reversible, endergonic addition of H_2 to the enamide−catalyst adduct, followed by turnover-limiting insertion of the alkene into a metal−hydrogen bond to form a metal alkyl. Our previous DFT investigations of the achiral [Rh(PH$_3$)$_2$]$^+$ catalyst supported the third scenario and were incompatible with the second.

Shedding light on the detailed mechanistic pathway of the catalytic asymmetric hydrogenation of dehydroamino acids requires a more realistic model system. Herein we report the full reaction surfaces for the [Rh((*R,R*)-Me-DuPHOS)]$^+$-catalyzed hydrogenation of α-formamidoacrylonitrile (**1**) (Figure 3) computed using the ONIOM method[32] to simulate a gas-phase reaction. A preliminary report of this work has already been published.[37]

(35) Armstrong, S. K.; Brown, J. M.; Burk, M. J. *Tetrahedron Lett.* **1993**, *34*, 879−882.

(36) Landis, C. R.; Brauch, T. W. *Inorg. Chim. Acta* **1998**, *270*, 285−297.

III. Computational Methods

Model System. We used the full (*R,R*)-Me-DuPHOS ligand as seen in Figure 3 for our calculations. To reduce the computational load, we used a model enamide, α-formamidoacrylonitrile (**1**), which contains a nitrile substituent on the α-position instead of the more traditional ester group. Knowles and co-workers previously found that hydrogenation of α-acetamidocinnamonitrile occurs with an enantiomeric excess (ee) comparable to that of methyl acetamidocinnamate using the DIPAMP catalyst,[33] thus demonstrating that nitrile-substituted enamides are appropriate models of the more common ester-substituted enamides. Preliminary computations involving carboxylic acid-substituted enamides further support this argument and will be the subject of a future publication.

ONIOM Details. The three geometry layers of the ONIOM calculation are shown in Figure 4. The core layer contains the reactive part of the catalyst system: the enamide, an ethylene-bridged diphosphine ligand (with hydrogens replacing the phospholane rings), rhodium, and the dihydrogen molecule (not shown in Figure 4). For this layer we use density functional theory (DFT), with Becke's three-parameter hybrid functional (B3),[38] and the Lee, Yang, and Parr correlation functional (LYP).[39] The B3LYP method has shown accuracy comparable to that of sophisticated post-Hartree−Fock (HF) methods in transition metal studies.[29,40] The intermediate layer includes the phospholane rings, without the methyl groups, and is treated with HF theory. The outer layer consists of the entire system and is modeled with the universal force field (UFF) molecular mechanics method.[41] An attempt to use a two-layer ONIOM, by treating the intermediate layer with UFF instead of HF, failed to reproduce critical aspects of crystallographic structures, particularly the P−Rh−P angle. Interestingly, UFF by itself reproduces the proper P−Rh−P angle, as does a full DFT optimization on the core.

All ONIOM calculations were performed with Gaussian98.[42] New atom types were needed to complete the Gaussian98 UFF force field, which could not accommodate coordinated olefins or square planar Rhodium complexes. Small UFF errors in the core are canceled in the ONIOM scheme; however, large errors can thwart the optimization, hence the need for additional atom types. Torsional contributions involving rhodium were set to zero. The Supporting Information contains all the code changes to Gaussian.

Geometry Optimization and Energies. ONIOM calculations are denoted by (High:Medium:Low), where High is the level of theory on the core, Medium is the level on the intermediate system, and Low is the level on the large system. All intermediates and transition states were initially optimized using (B3LYP/LANL2DZ:HF/LANL2MB:UFF), where LANL2DZ is the double-ζ quality, Hay and Wadt basis set for the valence and penultimate shells, with effective core potentials (ECPs) at rhodium[43] and phosphorus,[44] and a Dunning/Huzinaga full double-ζ basis on C, H, N, and O.[45] LANL2MB is the same collection of effective core potentials, but with the minimal STO-3G basis[46] on

(37) Landis, C. R.; Feldgus, S. *Angew. Chem., Int. Ed.* **2000**, *39*, 2863−2866.

(38) Becke, A. D. *Phys. Rev. A* **1988**, *38*, 3098−3100.

(39) Lee, C.; Yang, W.; Parr, R. G. *Phys. Rev. B* **1988**, *37*, 785−789.

(40) Brown, J. M.; Hofmann, P. *Organometallic Bonding and Reactivity: Fundamental Studies*; Springer-Verlag: Berlin, 1999.

(41) Rappé, A. K.; Casewit, C. J.; Colwell, K. S.; Goddard, W. A., III; Skiff, W. M. *J. Am. Chem. Soc.* **1992**, *114*, 10024−10035.

(42) Frisch, M. J.; Trucks, G. W.; Schlegel, H. B.; Scuseria, G. E.; Robb, M. A.; Cheeseman, J. R.; Zakrzewski, V. G.; Montgomery, J., J. A.; Stratmann, R. E.; Burant, J. C.; Dapprich, S.; Millam, J. M.; Daniels, A. D.; Kudin, K. N.; Strain, M. C.; Farkas, O.; Tomasi, J.; Barone, V.; Cossi, M.; Cammi, R.; Mennucci, B.; Pomelli, C.; Adamo, C.; Clifford, S.; Ochterski, J.; Petersson, G. A.; Ayala, P. Y.; Cui, Q.; Morokuma, K.; Malick, D. K.; Rabuck, A. D.; Raghavachari, K.; Foresman, J. B.; Cioslowski, J.; Ortiz, J. V.; Stefanov, B. B.; Liu, G.; Liashenko, A.; Piskorz, P.; Komaromi, I.; Gomperts, R.; Martin, R. L.; Fox, D. J.; Keith, T.; Al-Laham, M. A.; Peng, C. Y.; Nanayakkara, A.; Gonzalez, C.; Challacombe, M.; Gill, P. M. W.; Johnson, B.; Chen, W.; Wong, M. W.; Andres, J. L.; Gonzalez, C.; Head-Gordon, M.; Replogle, E. S.; Pople, J. A. *Gaussian 98, Revision A.6*; Gaussian, Inc.: Pittsburgh, PA, 1998.

(43) Hay, P. J.; Wadt, W. R. *J. Chem. Phys.* **1985**, *82*, 299−310.

(44) Hay, P. J.; Wadt, W. R. *J. Chem. Phys.* **1985**, *82*, 285−298.

(45) Dunning, T. H.; Hay, P. J. In *Modern Theoretical Chemistry*; Schaefer, H. F., Ed.; Plenum: New York, 1976; Vol. 3, p 1.

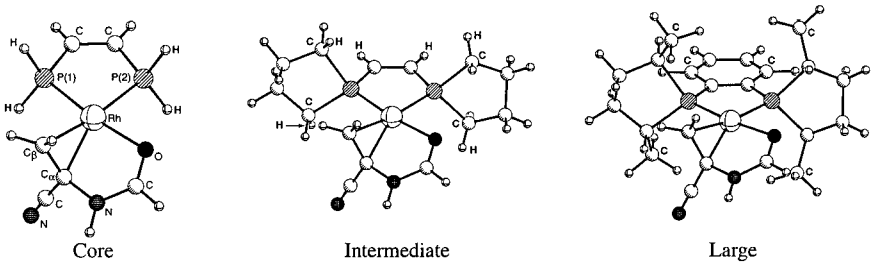

Figure 4. three different layers of the ONIOM calculation, shown here for **MIN**. Link atoms are shown in bold.

C, H, N, and O, and a minimal basis set on the valence and penultimate shells of rhodium and phosphorus. This level of theory will be referred to as basis I throughout this paper. For all structures, single-point energies were calculated using more sophisticated basis sets and effective core potentials from the Stuttgart group. The ECPs replaced 28 core electrons on rhodium and 10 on phosphorus. The Stuttgart valence basis sets used the following contraction schemes: (311111/22111/411) for rhodium[47] and (31/31) for phosphorus.[48] One d function with an exponent of 0.34 was added to phosphorus.[49] All other atoms used the 6-31G(d,p) basis set.[50−53] This level of theory, written in ONIOM notation as (B3LYP/Stuttgart:HF/LANL2MB:UFF), will be referred to as basis II throughout this paper.

Geometry reoptimizations with basis II were performed for all the structures along the most reactive pathway of each diastereomeric manifold (**A**) and some additional structures that displayed anomalous transition-state energies. In most cases, the difference in relative energy between a basis II energy on a basis I geometry (basis II//basis I) and a basis II reoptimized structure (basis II//basis II) was less than 0.5 kcal/mol; in a few cases there was an energy lowering of 1−2 kcal/mol (Table 1). The geometries of the reoptimized structures were almost identical to their basis I counterparts, with the exception of the Rh−P bond lengths, which were closer to the experimental values (see section III).

No symmetry or internal coordinate constraints were applied during optimizations. All reported intermediates were verified as true minima by the absence of negative eigenvalues in the vibrational frequency analysis. Transition-state structures (indicated by ‡) were located using the synchronous-guided quasi-Newton method (STQN) until the Hessian matrix had only one imaginary eigenvalue. ONIOM does not currently support intrinsic reaction coordinate calculations, so the identity of most transition states was confirmed by animating the negative eigenvector coordinate with a visualization program. When the mode was ambiguous, the structures were optimized (basis I) to minima in both directions along the negative eigenvalue coordinate.

Approximate free energies were obtained through thermochemical analysis of the frequency calculation, using the thermal correction to Gibbs free energy as reported by Gaussian98. This takes into account zero-point effects, thermal enthalpy corrections, and entropy. All energies reported in this paper, unless otherwise noted, are free energies at 298 K, using unscaled frequencies. All transition states are maxima on the electronic potential energy surface. These may not correspond to maxima on the free energy surface, and in fact, several transition states have a lower free energy than their corresponding intermediates. Reoptimization with basis II often solves this problem. We did not attempt to correct the free energy for hindered internal rotations.[54]

Table 1. Influence of Basis Set II on Electronic Energies Relative to **MAJ** + $\mathbf{H_2}$ (kcal/mol)

structure[a]	basis I/basis I	basis II/basis I	basis II/basis II
MIN + $\mathbf{H_2}$	4.4	4.5	4.6
IID-A	−0.7	−0.6	−0.2
IID-A‡	6.6	8.0	6.0
IID-A2	5.4	6.1	6.0
IID-A2‡	8.2	9.5	9.7
MOLH$_2$-A	6.7	5.7	5.2
MOLH$_2$-A‡	13.6	10.1	8.7
DIHY-A	5.3	5.7	5.7
DIHY-Aα‡	10.1	5.9	5.9
ALHY-Aα	−19.9	−20.9	−22.4
ALHY-Aα‡	−1.8	−2.6	−2.7
PROD-A	−28.0	−28.9	−29.2
iid-a	3.2	3.9	4.0
iid-a‡	4.0	4.7	4.9
molh$_2$-a	2.1	0.5	0.1
molh$_2$-b/d	11.6	12.6	10.4
molh$_2$-b‡	15.2	11.6	12.0
molh$_2$-d‡	11.0	12.2	12.7
molh$_2$-a‡	9.5	4.1	4.4
dihy-a	4.4	1.8	1.2
dihy-aα‡	6.6	2.0	2.2
alhy-a$_{trans}$α	−6.7	−12.1	−12.3
alhy-a$_{trans}$α‡	−6.5	−11.9	−12.2
alhy-aα	−21.7	−23.6	−24.8
alhy-aα‡	−3.8	−4.8	−4.8
prod-a	−27.7	−28.6	−28.9

[a] Acronyms are described in text.

IV. Computational Results

A. Overview of the Reaction Mechanism. The catalytic cycle computed for [Rh(Me-DuPHOS)(enamide)]$^+$ hydrogenation is similar to that calculated for the achiral system, [Rh(PH$_3$)$_2$(enamide)]$^+$.[31] The elementary steps of the cycle, the location of large barriers, and the relative energetics of intermediates and transition states are nearly identical for both chiral and achiral model systems. Both the chiral and achiral systems follow this sequence of elementary steps:

1. Formation of a square-planar cationic [Rh(bisphosphine)(enamide)]$^+$ adduct complex.

2. Addition of hydrogen to give a weakly bound ion−induced dipole species, denoted in this paper as **IID** and in the achiral system as **SQPL**.

3. Further addition of hydrogen to give stable five-coordinate molecular hydrogen complexes (**MOLH$_2$**).

4. Oxidative addition of hydrogen to generate a six-coordinate, pseudo-octahedral dihydride complex (**DIHY**).

5. Migratory insertion of an olefin carbon into a Rh−H bond to form a five-coordinate alkyl hydride (**ALHY**).

6. Reductive elimination of C−H from the alkyl hydride to produce the alkane product, coordinated to the catalyst (**PROD**).

(46) Hehre, W. J.; Stewart, R. F.; Pople, J. A. *J. Chem. Phys.* **1969**, *51*, 2657−2664.
(47) Andrae, D.; Haeussermann, U.; Dolg, M.; Stoll, H.; Preuss, H. *Theor. Chim. Acta* **1990**, *77*, 123−141.
(48) Bergner, A.; Dolg, M.; Kuenchle, W.; Stoll, H.; Preuss, H. *Mol. Phys.* **1993**, *80*, 1431−1441.
(49) Huzinaga, S. *Gaussian Basis Sets for Molecular Calculations*; Elsevier: Amsterdam, 1984.
(50) Ditchfield, R.; Hehre, W. J.; Pople, J. A. *J. Chem. Phys.* **1971**, *54*, 724−728.
(51) Hehre, W. J.; Ditchfield, R.; Pople, J. A. *J. Chem. Phys.* **1972**, *56*, 2257−2261.
(52) Hariharan, P. C.; Pople, J. A. *Theor. Chim. Acta* **1973**, *28*, 213−222.
(53) Hariharan, P. C.; Pople, J. A. *Mol. Phys.* **1974**, *27*, 209−214.
(54) Benson, S. W. *Thermochemical Kinetics*; John Wiley & Sons: New York, 1968.

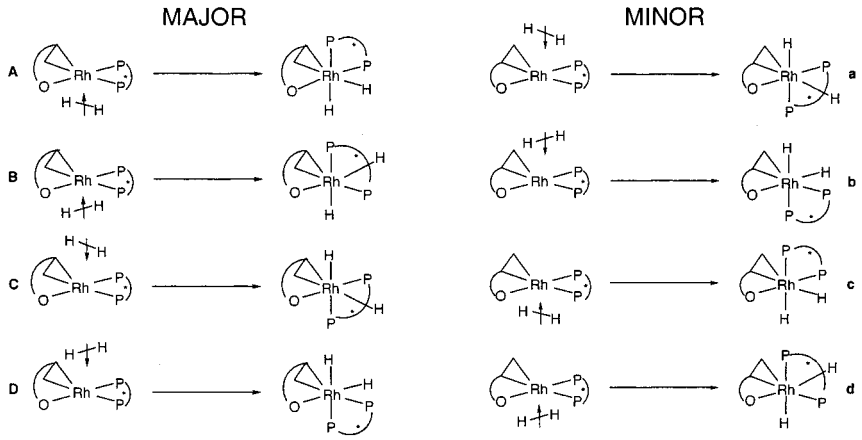

Figure 5. Eight potential dihydrides formed from cis addition of hydrogen to the catalyst−enamide adducts **MAJ** and **MIN**.

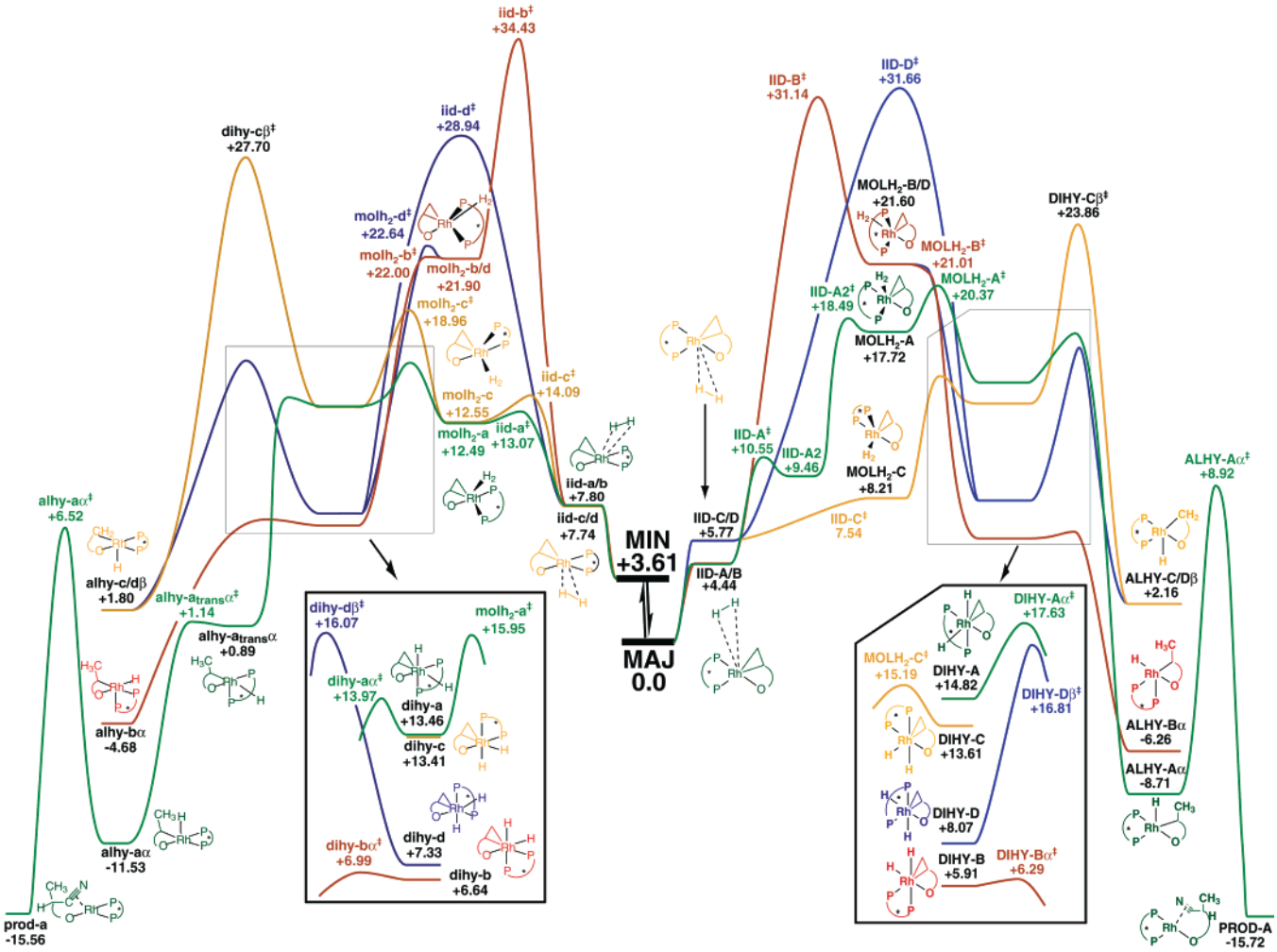

Figure 6. Free energy (kcal/mol) surface for the reaction of **MAJ** and **MIN** with H_2.

Our model does not include displacement of the alkane hydrogenation product from the catalyst nor association of substrate. Both of these processes involve substantial participation by solvent and/or the counterion and are not easily modeled.

This computed sequence of elementary steps agrees with previously published proposals on the mechanism of Rh(I)-catalyzed asymmetric hydrogenation.[4,5,18−25] For the DuPHOS system, this cycle occurs along two diastereomeric manifolds, corresponding to binding of the *re* or the *si* face of the olefin to the catalyst. In keeping with the nomenclature of Landis and Halpern,[25] we label the two manifolds MAJOR and MINOR, corresponding to the stability of the catalyst−enamide complexes (**MAJ** and **MIN**) formed in step 1. There are eight cis-addition pathways of hydrogen to the catalyst−enamide complexes, as shown in Figure 5. We denote these pathways as **A**, **B**, **C**, **D**, **a**, **b**, **c**, and **d**, using uppercase letters for the major manifold and lowercase letters for the minor manifold. We include an additional α or *β* designation for alkyl hydrides and their transition states, to distinguish between the formation of Rh−C bonds at the α and *β* carbons of formamidoacrylonitrile.

Figure 6 shows the free energy surface for both diastereomeric manifolds along all eight isomeric pathways. Figures 7 and 8

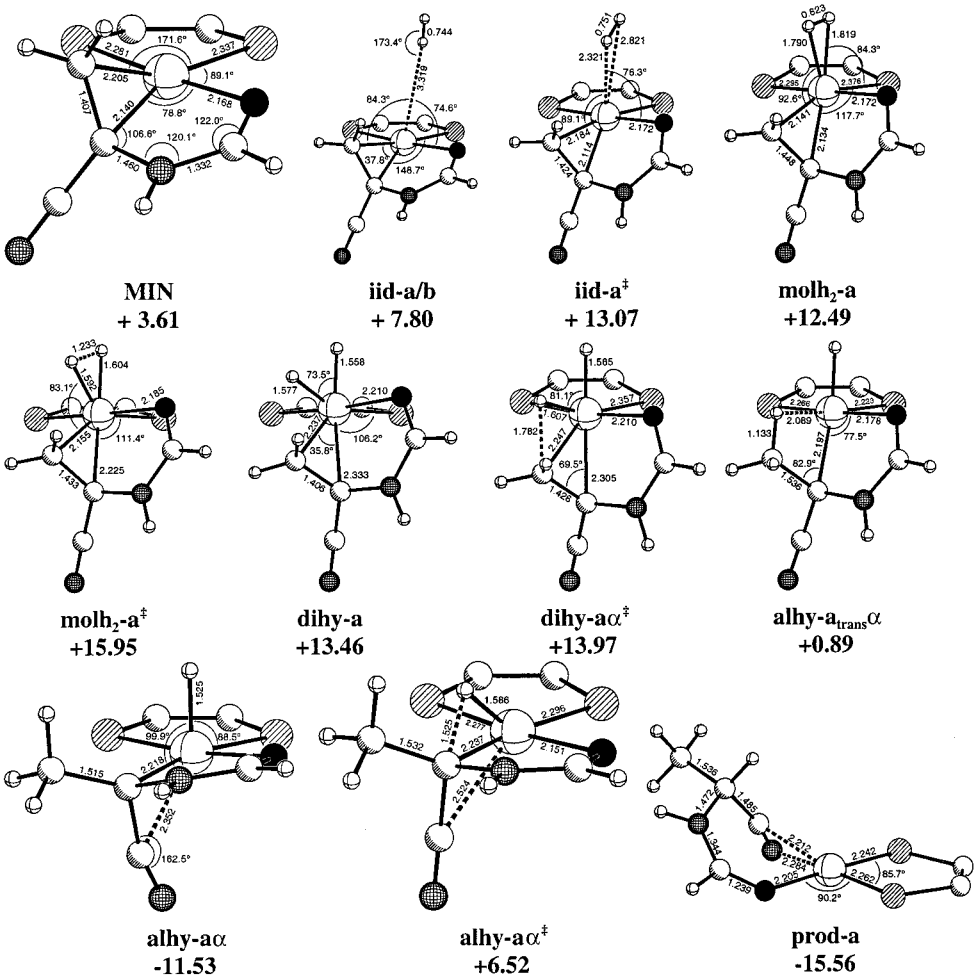

Figure 7. Optimized geometries and free energies in kilocalories per mole (at the basis II/basis II level) for the reactive pathway on the minor manifold. The phospholane rings and the rest of the benzene backbone are removed for clarity.

depict the optimized structures along the reactive pathway for the minor (**a**) and major (**A**) manifolds, respectively. All three figures report free energies in kilocalories per mole; we define the energy of **MAJ** + $\mathbf{H_2}$ (infinitely separated) to be 0 kcal/mol. The electronic energies for all structures are given in Table 2. Cartesian coordinates and additional energetic details for all structures can be found in the Supporting Information.

B. Structures and Energetics of Rh−Alkene Complexes. Three [Rh(enamide)(diphosphine)]$^{+}$ crystal structures have been published over the last 21 years: [Rh(DIPHOS)(methyl (*Z*)-α-acetamidocinnamate)](BF_4),[22] [Rh((*S,S*)-CHIRAPHOS)(ethyl (*Z*)-α-acetamidocinnamate)](ClO_4),[23] and [Rh((*R,R*)-DIPAMP)-(methyl (*Z*)-*β*-propyl-α-acetamidoacrylate)](BF_4)[55] (CHIRAPHOS = 2,3-bis(diphenylphosphino)butane; DIPAMP = 1,2-bis(phenyl-*o*-anisylphosphino)ethane). One crystal structure containing Me-DuPHOS has been published: [(cyclooctadiene)-Rh((*S,S*)-Me-DuPHOS)](SbF_6).[10] Structural data for the catalyst−enamide complexes (**MAJ**, **MIN**) are collected alongside empirical structural data in Table 3. The calculated lowest energy conformation of the DuPHOS ligand is shown in Figure 9. The calculated bond lengths and angles show reasonable agreement with experimental data. The Rh−P bond trans to the coordinated olefin is longer than the Rh−P bond trans to the coordinated amide carbonyl, reproducing the expected trans influences of these ligands. The largest discrepancies appear in Rh−P and P−C bond lengths, which are up to 0.14 Å too long in the calculated structures. Reoptimizing with basis II shortens all phosphorus bond lengths, with the largest deviation from empirical data being 0.06 Å. Use of basis II also significantly improves the Rh−P−C angles of the coordinated DuPHOS ligand.

The MAJOR catalyst−enamide diastereomer is 3.6 kcal/mol lower in energy than the MINOR, corresponding to a [**MAJ**]:[**MIN**] ratio of 500:1 at 298 K. A ^{31}P NMR study of [((*S,S*)-Me-DuPHOS)Rh(methyl α-acetamidocinnamate)]$^{+}$ was unable to detect any minor diastereomer,[35] indicating its equilibrium concentration to be less than 1%, consistent with our calculated values. The primary structural difference between the two diastereomers lies in the identity of the olefinic carbon in the Rh−diphosphine plane. The major diastereomer has the α-carbon very nearly in the Rh−P−P plane (α, 9.3° out of plane; *β*, 31.3° out of plane), whereas the minor diastereomer has the *β*-carbon in the plane (α, 15.1° out of plane; *β*, 5.1° out of plane). The disposition of the α-carbon in **MAJ** is consistent with the three known crystallographic structures of enamides bound to [Rh(bisphosphine)]$^{+}$ cores (each corresponding to the more stable diastereomer/conformer). Angles made by the Rh−C vector and the P−Rh−P plane are as follow:

ligand	Rh−Cα (°)	Rh−C*β* (°)
CHIRAPHOS[23]	0.5	21.6
DIPAMP[55]	5.5	22.0
DIPHOS[22]	2.8	18.1

There are several other notable differences between the com-

(55) McCulloch, B.; Halpern, J.; Thompson, M. R.; Landis, C. R. *Organometallics* **1990**, *9*, 1392−1395.

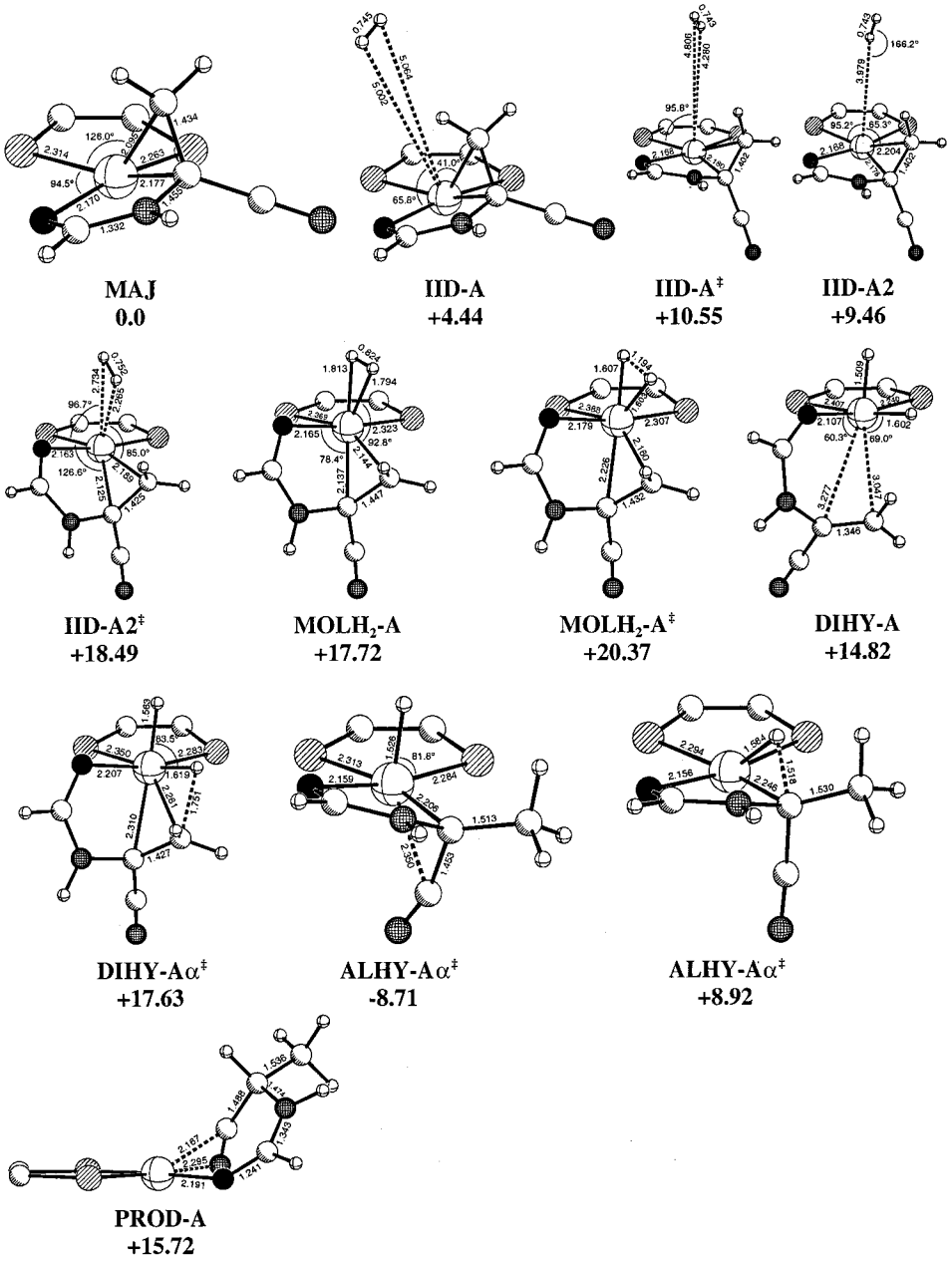

Figure 8. Optimized geometries and free energies in kilocalories per mole (at the basis II/basis II level) for the reactive pathway on the major manifold. The phospholane rings and the rest of the benzene backbone are removed for clarity.

puted structures of **MAJ** and **MIN**. The Rh−C_α distance is slightly longer in **MAJ** (2.177 Å in **MAJ** vs 2.140 Å in **MIN**), whereas the Rh−C_β distance is considerably longer in **MIN** (2.095 vs 2.205 Å). In both cases, the out-of-plane carbon has a shorter bond to rhodium. The C−C bond distance is longer in **MAJ** (1.434 vs 1.407 Å). The Rh−P bonds in **MAJ** are slightly longer than those in **MIN** (2.264 and 2.314 vs 2.281 and 2.337 Å), with shorter bonds for the phosphorus atoms trans to C═C. Overall, Rh−olefin binding in the major diastereomer appears stronger, with considerably more Rh → olefin backbonding (more metallacyclopropane character), than in the minor diastereomer. The lowest energy phospholane ring conformations of the DuPHOS ligand are the same for both diastereomers.

C. Formation of Ion−Induced Dipole (IID) Complexes. The initial addition of H_2 to the cationic catalyst−enamide complex occurs with very small changes in geometry and energy. Formation of all initial **IID** complexes is slightly exothermic (ca. − 0.6 kcal/mol at basis I and basis II levels) but considerably endergonic (4−6 kcal/mol), due to the partial

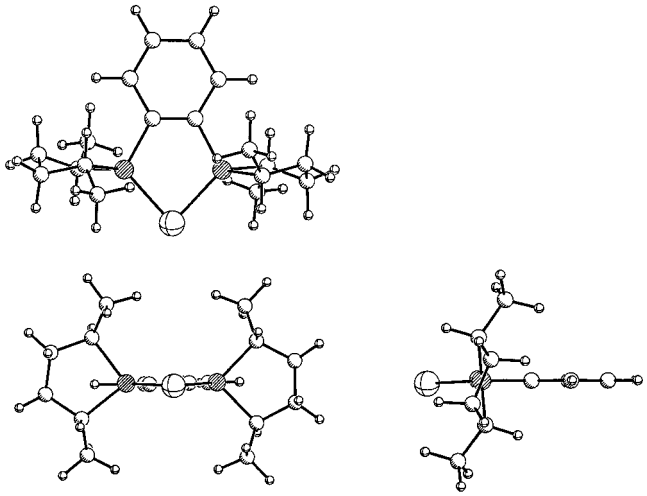

Figure 9. Structural drawing of (*R*,*R*)-Me-DuPHOS ligand, showing the lowest energy conformation of phospholane rings.

Table 2. Relative Electronic Energies (kcal/mol) for Minor (Left) and Major (Right) Manifolds, Relative to **MAJ** + H_2[a]

MIN + H_2	4.57	**MAJ** + H_2	0.00
iid-a/b	3.97	**IID-A/B**	−0.18
iid-c/d	3.94	**IID-C/D**	−0.39
iid-a‡	4.88	**IID-A**‡	5.99
iid-b‡	23.17	**IID-A2**	5.97
iid-c‡	6.49	**IID-A2**‡	9.67
iid-d‡	18.98	**IID-B**‡	19.97
molh$_2$-a	0.13	**IID-C**‡	−0.07
molh$_2$-b/d	10.44	**IID-D**‡	21.08
molh$_2$-c	1.26	**MOLH$_2$-A**	5.24
molh$_2$-a‡	4.41	**MOLH$_2$-B/D**	10.43
molh$_2$-b‡	12.01	**MOLH$_2$-C**	−3.09
molh$_2$-c‡	8.08	**MOLH$_2$-A**‡	8.95
molh$_2$-d‡	12.70	**MOLH$_2$-B**‡	11.84
dihy-a	1.24	**MOLH$_2$-C**‡	4.20
dihy-b	−5.21	**MOLH$_2$-D**‡	12.32
dihy-c	4.77	**DIHY-A**	5.74
dihy-d	−4.00	**DIHY-B**	−6.07
dihy-a$\alpha^‡$	2.16	**DIHY-C**	1.85
dihy-b$\alpha^‡$	−4.03	**DIHY-D**	−3.22
dihy-c$\beta^‡$	17.43	**DIHY-A**$\alpha^‡$	5.89
dihy-d$\beta^‡$	6.20	**DIHY-B**$\alpha^‡$	−4.69
alhy-a$_{trans}\alpha$	−12.29	**DIHY-C**$\beta^‡$	13.69
alhy-a$_{trans}\alpha^‡$	−12.16	**DIHY-D**$\beta^‡$	6.66
alhy-aα	−24.79	**ALHY-A**α	−22.37
alhy-bα	−17.25	**ALHY-B**α	−18.55
alhy-c/dβ	−10.42	**ALHY-C/D**β	−10.31
alhy-a$\alpha^‡$	−4.79	**ALHY-A**$\alpha^‡$	−2.67
prod-a	−28.87	**PROD-A**	−29.23

[a] All structures on pathway **A** are reoptimized with basis II, and energies are reported relative to reoptimized starting points. **molh$_2$-b/d**, **molh$_2$-b**‡, and **molh$_2$-d**‡ also are reoptimized.

loss of dihydrogen translational and rotational entropy. The principal difference between the structures is the Rh−H_2 distance, which varies from 2.9 Å for **IID-C/D** to nearly 5.1 Å for **IID-A/B**, depending on the steric crowding at the face H_2 approaches.

Two ion−induced dipole complexes are formed along major pathway **A**. For the initial complex, **IID-A/B**, H_2 is blocked from the catalyst by one of the DuPHOS methyl groups and the β-carbon, hence the large Rh−H_2 distance of >5.0 Å. A higher energy intermediate, **IID-A2**, has the β-carbon pushed down into the plane and H_2 approximately 4 Å directly above rhodium. This intermediate will have important consequences for the reactivity of the major diastereomer (vide infra).

D. Conversion of Ion−Induced Dipole Complexes into Molecular H_2 (MOLH$_2$) Complexes. A striking feature of our study of the achiral $[Rh(PH_3)_2]^+$ catalyst was the existence of stable five-coordinate molecular hydrogen complexes that exerted a profound influence on the reactivity of certain pathways. Similar qualitative and quantitative results are found from ONIOM computations of the $[Rh(DuPHOS)]^+$ catalyst. The six diastereomeric molecular hydrogen compounds exhibit trigonal bipyramidal geometry, each with the electronegative amido oxygen occupying an axial position, mirroring a common feature of main group trigonal bipyramidal structures. We were able to locate several four-coordinate intermediates, in which the coordinated C═C was displaced by H_2, but none of these led to low-energy reactive pathways.

Rationalization of the relative stabilities of the different molecular H_2 complexes follows our previous lines of reasoning. There is a clear preference for H_2 to be in the equatorial plane (**A** and **C**) instead of the axial position (**B/D**), and the double bond is found to be equatorial in all structures. Extended Hückel computations by Hoffmann and Rossi[56] found that, in five-coordinate d^8 transition metal complexes, strong σ-donor ligands prefer the axial site, but π-acceptor ligands prefer to be equatorial. Hartree−Fock computations by Morokuma et al.[57] found a strong preference for ethylene to be equatorial in Rh(H)(C_2H_4)(CO)$_2$(PH_3). Burk et al.[58] and Sargent and Hall[59] find that this trend holds, experimentally and computationally, for d^8 Ir complexes. Complex **B/D** is further destabilized by the diequatorial arrangement of the phosphorus atoms, which have a natural P−Rh−P bite angle (∼85°) that is too small to accommodate the idealized 120° equatorial bond angle.

The energetic barriers for approach of H_2 along the P−Rh−C axis (**A** and **C**) and along the P−Rh−O axis (**B** and **D**) differ enormously. For approach along the Rh−C bond, the barriers are small, with most of the free energy penalty coming from the loss of H_2 entropy. In contrast, approach along the P−Rh−O axis is strongly disfavored (>30 kcal/mol for **IID-B**‡ and **iid-b**‡). We rationalize these results with a least-motion argument.[60] Formation of a trigonal bipyramidal intermediate with H_2 trans to O requires both phosphorus atoms to move out of the original coordination plane while H_2 migrates into that plane from a perpendicular direction. Such extensive nuclear and electronic reorganization generates a large barrier. The existence of similar barrier heights in the sterically unhindered [Rh-

Table 3. Comparison of Computational and Empirical Structural Data for Starting Complexes

	X-tal 1−3[a]	X-tal 4[b]	**MIN**[e] (basis I)	**MIN**[c] (basis II)	**MAJ**[c] (basis I)	**MAJ**[c] (basis II)
			Bonds (Å)			
Rh−O	2.12(1)		2.147	2.168	2.146	2.170
Rh−Cα	2.18(2)		2.147	2.140	2.176	2.177
Rh−Cβ	2.22(3)		2.200	2.205	2.097	2.095
Rh−P$_{trans}$O	2.23(1)	2.263(2)	2.369	2.281	2.348	2.264
Rh−P$_{trans}$C	2.28(1)	2.273(2)	2.413	2.337	2.392	2.314
Cα−Cβ	1.38(1)		1.426	1.407	1.453	1.434
P(1)−C(5)		1.809(8)	1.878	1.851	1.866	1.836
P(2)−C(6)		1.816(7)	1.863	1.832	1.874	1.848
			Angles (°)			
O−Rh−Cα	77.9(1)		79.1	78.8	78.4	78.1
Cα−Rh−Pcis	109(1)		107.2	107.8	104	105.2
P−Rh−P	83.0(1)	84.73(7)	84.5	84.4	84.9	84.7
O−Rh−Pcis	90(2)		88.9	89.1	94.6	94.5
Cα−Rh−Cβ	36.5(5)		38.3	37.7	39.7	39.2
Rh−P(1)−C(5)		111.0(3)	107.8	109	107.7	109.1
Rh−P(2)−C(6)		109.6(2)	108.1	109.5	108.3	109.8

[a] Averages of three crystallographic structures: [Rh(DIPHOS)(methyl (*Z*)-α-acetamidocinnamate)](BF_4)[22] [Rh((*S*,*S*)-CHIRAPHOS)(ethyl (*Z*)-α-acetamidocinnamate)](ClO_4)[23] [Rh((*R*,*R*)-DIPAMP)(methyl (*Z*)-β-propyl-α-acetamidoacrylate)](BF_4)[55]. [b] [(COD)Rh((*S*,*S*)-Me-DuPHOS)](SbF_6).[10] [c] Optimized with basis set given in parentheses.

$(PH_3)_2]^+$ system indicates that the barriers have an electronic, rather than steric, origin.

We were unable to find transition states connecting the ion−induced dipole complex and the molecular hydrogen complex along pathway **D** on either manifold. Instead, we found high-energy transition states for the direct oxidative addition of hydrogen to form the dihydrides (**IID-D**‡, 31.66 kcal/mol; **iid-d**‡, 28.94 kcal/mol). This is the only example that we found of dihydride formation without a molecular H_2 intermediate. Dihydride **D** also may be formed through the intermediacy of **MOLH$_2$-B/D**.

E. Conversion of Molecular H_2 Complexes to Metal Dihydrides. Eight dihydride diastereomers could result from the oxidative addition of H_2 to **MAJ** and **MIN**. We find all eight reactions to be endergonic, with free energies ranging from +5.9 kcal/mol (**DIHY-B**) to +14.8 kcal/mol (**DIHY-A**). The relative ordering of the dihydride energies is the same in both manifolds (**B** < **D** ≪ **C** < **A**), which is nearly the order found previously for $[Rh(PH_3)_2]^+$, but with **C** and **A** swapped. The corresponding dihydrides on the major and minor manifolds have very similar energies: the average difference between the pairs (**DIHY-A**, **dihy-a**), (**DIHY-B**, **dihy-b**), etc. is less than 1 kcal/mol.

Each of the eight dihydride diastereomers has a hydrogen trans to a phosphorus. The low-energy dihydrides place the remaining hydrogen trans to oxygen (**B** and **D**), while the high-energy dihydrides have a hydrogen trans to the C−C double bond (**A** and **C**). This ordering of energies is consistent with expected trans influences: the double bond has a higher trans influence than the amido oxygen and prefers not to be trans to the hydride ligand, which has the highest trans influence. The computed geometries demonstrate the strong trans influence of the hydride with very long Rh−olefinic C distances in **DIHY-A** (3.05 Å) and **dihy-c** (2.92 Å).

We find low barriers for the oxidative addition step. The **C** pathways have the largest barriers (6.98 kcal/mol barrier along **C**; 6.41 kcal/mol barrier along **c**). The oxidative addition barriers for **B** and **D** are extremely small. Negative free energy barriers, a minor computational artifact, are observed for the oxidative addition reactions involving **MOLH$_2$-B**‡ and **MOLH$_2$-D**‡. This artifact stems from the computation of transition-state single-point energies with a larger basis set than was used for the geometry optimization. Reoptimization with basis II, which was done for **molh$_2$-b**‡ and **molh$_2$-d**‡, generates very small positive barriers. Despite the small oxidative addition barriers along paths **B** and **D** and the thermodynamic stability of the dihydrides, dihydrides **B** and **D** are kinetically unimportant, due to the large barriers preceding formation of the molecular hydrogen complexes. Again, these results were anticipated on the basis of our previous computations of $[Rh(PH_3)_2]^+$ catalysts.

As is clearly revealed by Figure 6, the overall rates of dihydride formation along the **MAJ** and **MIN** manifolds do not correlate with the thermodynamics of dihydride formation. This result, which runs counter to previous suggestions,[2] emphasizes the critical importance of understanding the kinetics of elementary steps in catalytic processes. Of course, this is not a surprise since catalysis is wholly a kinetic phenomenon.

F. Conversion of Dihydrides into Alkyl Hydrides. We find that seven alkyl hydride intermediates form directly from the dihydrides through migratory insertion of the C−C bond into a Rh−H bond. These alkyl hydrides can be split into two classes: α-alkyl hydrides (pathways **A** and **B**) and *β*-alkyl hydrides (pathways **C** and **D**). All of the alkyl hydrides have a monovacant octahedral structure. Six have the remaining hydride cis to the alkyl. One alkyl hydride, **alhy-a$_{trans}$α**, has the hydride trans to the alkyl and is 12.4 kcal/mol higher in energy than its cis counterpart, reflecting the strong trans avoidance of hydride and alkyl ligands. There is a very low energy barrier (0.25 kcal/mol) for isomerization of **alhy-a$_{trans}$α** to **alhy-aα**. Presumably, the corresponding alkyl hydride on the major diastereomer pathway, **ALHY-A$_{trans}$α**, forms a similarly shallow well that we were unable to locate.

The relative energetics of the alkyl hydride intermediates follow trends seen for the $[Rh(PH_3)_2]^+$ model catalyst. That is, we find that *β*-alkyl hydrides are intrinsically disfavored by at least 10 kcal/mol relative to α-alkyl hydrides. However, it is likely that these energy differences may be significantly altered by changing the electronic nature of the substituents in the α and *β* positions. The barriers for insertion to form α-alkyl hydrides are very low, with the largest being **DIHY-Aα**‡ (2.81 kcal/mol) and the rest being less than 0.5 kcal/mol. Insertion to form *β*-alkyl hydrides, on the other hand, is considerably more difficult. Pathways **D** and **d** have barriers of about 9 kcal/mol, and pathways **C** and c, which have trans H−Rh−C structures at the transition state, have even higher barriers (**DIHY-C*β***‡, 10.2 kcal/mol; **dihy-c*β***‡, 14.3 kcal/mol).

G. Alkyl Hydride Reductive Elimination. Reductive elimination of the alkyl hydride to yield hydrogenated product coordinated to the catalyst is the final elementary step in our computational model. We examined only the reductive elimination pathways corresponding to the thermodynamically and kinetically favored alkyl hydrides **ALHY-Aα** and **alhy-aα**. The reactions occur through hydride migration transition states **ALHY-Aα**‡ and **alhy-aα**‡, with barriers relative to the alkyl hydride intermediates of 17.2 and 18.0 kcal/mol, respectively. Both reactions are exergonic: 7.8 kcal/mol to form **PROD-A**, and 4.5 kcal/mol to form **prod-a**.

H. Overview of the Computational Results. Figure 6 summarizes the relative energetics of the various intermediates and transition states along the catalytic pathway and illustrates several key conclusions:

(1) Pathway **B** is blocked on both manifolds by large barriers to formation of the molecular hydrogen complexes.

(2) Pathway **D** is blocked on both manifolds by large barriers to formation of the dihydrides, either directly or through the **B/D** molecular hydrogen complex.

(3) Pathway **C** is blocked on both manifolds by large barriers for migratory insertion to form the alkyl hydride.

(4) Pathway **A** has the lowest overall barriers on both manifolds.

(5) The activation free energy for reaction along **A** on the major manifold is 20.4 kcal/mol but only 15.9 kcal/mol on the minor manifold. Thus, ONIOM computations reproduce the anti-lock-and-key motif: the less stable diastereomer reacts with dihydrogen considerably faster than the more stable one.

(6) Migratory insertion to form **alhy-a$_{trans}$α** has a lower barrier than reductive elimination of H_2 from **dihy-a** to form **molh$_2$-a**, meaning the reaction can be considered as a rapid, endergonic preequilibrium between **MIN** and **molh$_2$-a**, followed by turnover-limiting and irreversible oxidative addition to form **dihy-a**. This is a significant departure from the conclusions of

(56) Rossi, A. R.; Hoffmann, R. *Inorg. Chem.* **1975**, *14*, 365−374.
(57) Koga, N.; Jin, S. Q.; Morokuma, K. *J. Am. Chem. Soc.* **1988**, *110*, 3417−3425.
(58) Burk, M. J.; McGrath, M. P.; Wheeler, R.; Crabtree, R. H. *J. Am. Chem. Soc.* **1988**, *110*, 5034−5039.
(59) Sargent, A. L.; Hall, M. B. *Inorg. Chem.* **1992**, *31*, 317−321.
(60) Lowry, T. H.; Richardson, K. S. *Mechanism and Theory in Organic Chemistry*, 2nd ed.; Harper & Row: New York, 1981.

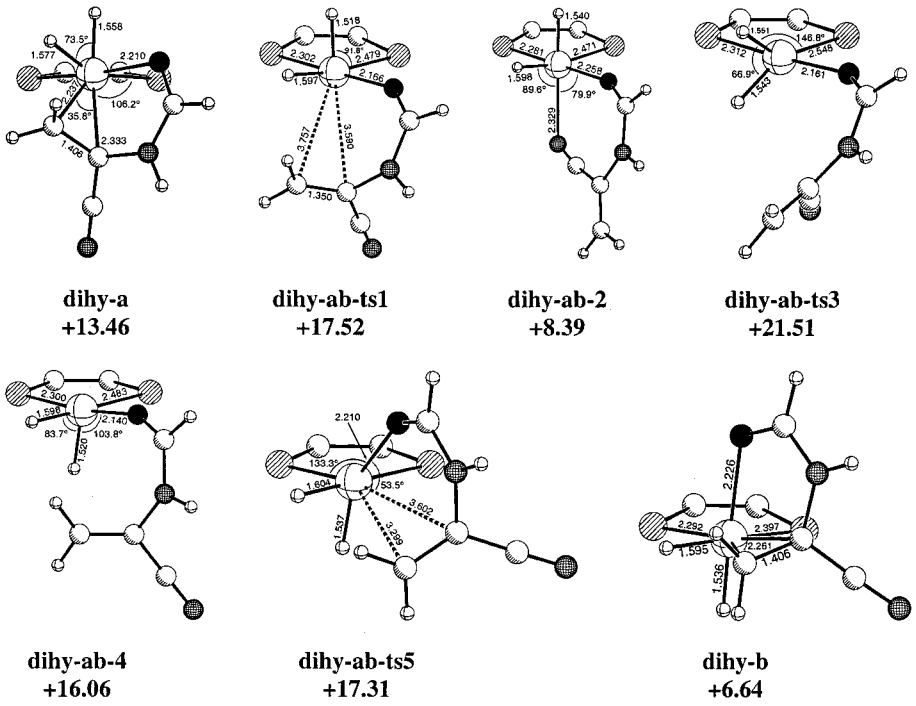

Figure 10. Structures and energies for the **dihy-a** → **dihy-b** isomerization pathway. Structures for **dihy-a** and **dihy-b** were reoptimized using basis II. The other structures were not.

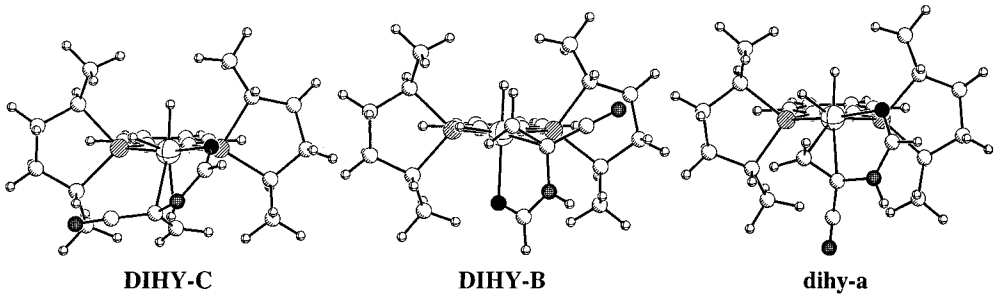

Figure 11. Geometries of relevant dihydrides for isomerization pathways.

our $[Rh(PH_3)_2]^+$ study, for which we found migratory insertion, not oxidative addition, to be turnover limiting. Therefore, we conclude that the relative barrier heights for oxidative addition and migratory insertion are sensitive to the stereoelectronic environment in a way that cautions against generalization to other systems.

I. Isomerization Pathways. The above discussion assumes no competitive mechanism for isomerization between different pathways. In a previous paper, we showed that isomerization among molecular hydrogen complexes was a relatively high-energy process.[31] More likely would be interpathway isomerization of the dihydride intermediates via dissociation of the C−C double bond from rhodium. For the achiral $[Rh(PH_3)_2]^+$ system, our primary concern was isomerization from **DIHY-A** to **DIHY-B**, which could have changed the identity of the turnover-limiting step. For [Rh(Me-DuPHOS)(α-formamidoacrylonitrile)]$^+$ computations, we first focus on the isomerization pathway connecting **dihy-a** to **dihy-b**, which serves as a model for all potential dihydride isomerizations. Optimized structures and transition states for the isomerization pathway are shown in Figure 10. The large barrier for the hydrogen site isomerization (transition state **dihy-ab-ts3**) precludes dihydride isomerization from competing with migratory insertion.

A second concern is the potential isomerization of **DIHY-C** to **DIHY-B** or **DIHY-D**, which would render the major manifold more reactive than the minor. The **DIHY-C** → **DIHY-D** transformation will encounter a barrier similar to that of **dihy-a** → **dihy-b**: the high-energy hydrogen site isomerization, with a barrier of approximately 13 kcal/mol. **DIHY-C** → **DIHY-B**, on the other hand, is different. It can be seen from Figure 11 that isomerization from **DIHY-C** to **DIHY-B** requires dissociation of the coordinated alkene, rotation around the Rh−O bond to adopt a configuration similar to that of **dihy-ab-4**, oxygen site isomerization similar to that of **dihy-ab-ts5**, and reassociation of the alkene. Although we have not performed detailed computations on this isomerization process, we can reasonably assume that the combination of alkene dissociation and site isomerization will be too slow to compete with direct reaction along pathway **a**. More detailed analyses of such isomerization processes are complicated by the likely involvement of solvent and/or counterion and the possibility of crossover between major and minor manifolds.

J. Calculated Isotope Effects. Kinetic isotope effects (KIEs) are powerful experimental probes of transition states. In many instances, KIEs can distinguish between competing kinetic models. ONIOM calculations for the hydrogenation of [Rh(Me-DuPHOS)(α-formamidoacrylonitrile)]$^+$ indicate a rapid, reversible, endergonic pre-equilibrium between the catalyst−enamide complex and a molecular hydrogen complex, followed by turnover-limiting oxidative addition. We have calculated isotope effects using the method of Krogh-Jespersen et al.[61,62] If oxidative addition is turnover limiting, the observed KIE will

Table 4. Computed Equilibrium Isotope Effects (EIE), Forward Kinetic Isotope Effects (KIE), and Tunneling Corrections (TC) for H_2 vs D_2 along the Reaction Pathway

transformation	K (EIE)	k^f (KIE)	TC[a]
MAJ → MOLH$_2$-A	0.625		
MIN → molh$_2$-a	0.615		
MOLH$_2$-A → DIHY-A	1.108	2.214	1.612
molh$_2$-a → dihy-a	1.049	2.575	1.800
DIHY-A → ALHY-Aα		1.556	1.172
dihy-a → dihy-aα		1.561	1.119

[a] Tunneling correction to KIE calculations are presented but not factored into the forward kinetic isotope effects.

Table 5. Computed Equilibrium Isotope Effects (EIE), Forward Kinetic Isotope Effects (KIE), and Tunneling Corrections (TC) for Isomers Resulting from HD Addition along Pathway **A**

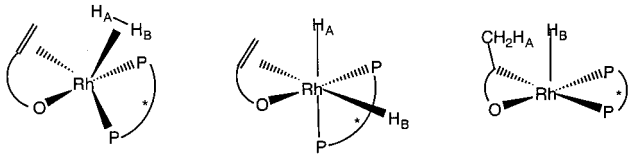

transformation	$(K_{H_AD_B})/(K_{D_AH_{AB}})$ (EIE)	$(k_{H_AD_B}{}^f)/(k_{D_AH_B}{}^f)$ (KIE)	TC[a]
MAJ → MOLH$_2$-A	1.022		
MIN → molh$_2$-a	0.937		
MOLH$_2$-A → DIHY-A	1.194	1.043	1.046
molh$_2$-a → dihy-a	1.197	1.072	1.087
DIHY-A → ALHY-Aα		1.421	1.157
dihy-a → alhy-aα		1.451	1.107

[a] Tunneling correction to KIE calculations are presented but not factored into the forward kinetic isotope effects.

be the product of the equilibrium isotope effect (EIE) for molecular hydrogen formation and the KIE for oxidative addition. If migratory insertion is rate limiting, the observed KIE will be the product of the EIEs for molecular hydrogen and dihydride formation and the KIE for migratory insertion.

Table 4 shows the calculated isotope effects for each step (tunneling corrections are presented but not used in the computation of observed isotope effects). For the case of turnover-limiting oxidative addition, the computed isotope effects are

Minor Pathway **a**: $(0.615)(2.575) = 1.584$

Major Pathway **A**: $(0.625)(2.214) = 1.384$

For turnover-limiting migratory insertion, the computed isotope effects are

Minor Pathway **a**: $(0.615)(1.049)(1.561) = 1.007$

Major Pathway **A**: $(0.625)(1.108)(1.556) = 1.077$

The KIEs can also be used to predict site preferences for HD hydrogenation, i.e., whether D is preferentially found in the α or β position. Table 5 shows EIEs and KIEs for various HD isomers. If oxidative addition is turnover limiting, the calculated $(\alpha_H\beta_D)/(\alpha_D\beta_H)$ isotope effects are

Minor Pathway **a**: $(0.937)(1.072) = 1.004$

Major Pathway **A**: $(1.022)(1.043) = 1.066$

whereas turnover-limiting migratory insertion leads to HD/DH isotope effects of

Minor Pathway **a**: $(0.937)(1.197)(1.451) = 1.627$

Major Pathway **A**: $(1.022)(1.194)(1.421) = 1.734$

These values are similar to previous computations for the hydrogenation of $[Rh(PH_3)_2(\alpha\text{-formamidoacrylonitrile})]^+$.[31] The experimental H_2/D_2 kinetic isotope effects for hydrogenation of prochiral enamides with a [Rh(DIPHOS)] catalyst are small (1.04[36]−1.22[20]), and there is a sizable preference for D to occupy the α position instead of the β position (1.21[36]−1.35[20,36]). Unfortunately, the few experimental results generally lie midway between the limiting extremes determined by computation. Furthermore, we have found that the relative barriers of oxidative addition and migratory insertion are sensitive to stereoelectronic influences of the phosphine ligand; thus, we cannot reliably extrapolate previous experimental results to the DuPHOS-ligated catalysts. Therefore, resolution of computational and experimental KIEs awaits further collection of experimental data or computations on systems for which KIE experiments have been performed. It should be noted that, even if insertion along the **A** pathways were turnover-limiting for the [Rh(Me-DuPHOS)(α-formamidoacrylonitrile)]$^+$ system, the computations again predict an anti-lock-and-key motif, with a difference in diastereomeric transition-state energies that exceeds 3.5 kcal/mol, as shown in Figure 6.

V. Conclusions

We emphasize that our computations concern model systems in the gas phase and in the absence of counterions. Efficiencies gained by these approximations are offset by limitations: we are not able to estimate equilibrium constants, association barriers, or dissociation barriers for reactions such as the binding of enamides to solvated [(diphosphine)Rh]$^+$, nor are we able to probe the influence of solvent coordination on reductive elimination rates or interpathway isomerizations. At this time, our computational models are limited to control of enantioselectivity along a commonly accepted reaction pathway. The computational model has accuracy limitations, also. For comparisons of diastereomers, cancellation of errors makes accuracies within 1−2 kcal/mol likely. For absolute energies, such as activation enthalpies, we estimate error ranges of 3−4 kcal/mol.

A. The Difference in Diastereomer Stabilities and Reactivities. Reproducing the anti-lock-and-key behavior of catalytic asymmetric hydrogenation is, by itself, a significant accomplishment for computational transition metal chemistry and the ONIOM method. However, simple models for the origin of the anti-lock-and-key behavior have greater general utility. We begin by developing a simple model for the relative stabilities ($\Delta\Delta G°$ = 3.6 kcal/mol) of **MAJ** and **MIN**. The major structural difference between the two complexes, as can be seen in Figures 7 and 8, is the identity of the olefin carbon in the rhodium−diphosphine plane: α-carbon in the major diastereomer, β-carbon in the minor. Replacement of the methyl groups of the DuPHOS phospholane ring with hydrogens and reoptimization of the structures results in both diastereomers having the α-carbon in the plane, as shown in Figure 12. Clearly, there is an intrinsic electronic preference for the α-carbon to be in the plane. Preliminary results indicate that the magnitude of the preference for the α-C to lie in the P−Rh−P coordination plane varies significantly with the steric and electronic properties of

(61) Abu-Hasanayn, F.; Krogh-Jespersen, K.; Goldman, A. S. *J. Am. Chem. Soc.* **1993**, *115*, 8019−8023.

(62) Abu-Hasanayn, F.; Goldman, A. S.; Krogh-Jespersen, K. *J. Phys. Chem.* **1993**, *97*, 5890−5896.

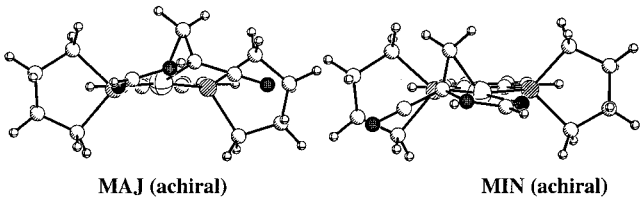

Figure 12. Optimized geometries for the major (**MAJ**) and minor (**MIN**) diastereomeric catalyst−enamide adducts upon replacement of the DuPHOS methyl groups with hydrogens to give achiral diphosphines. For these structures, **MIN** is essentially equal in energy to **MAJ** (ΔE = 0.15 kcal/mol).

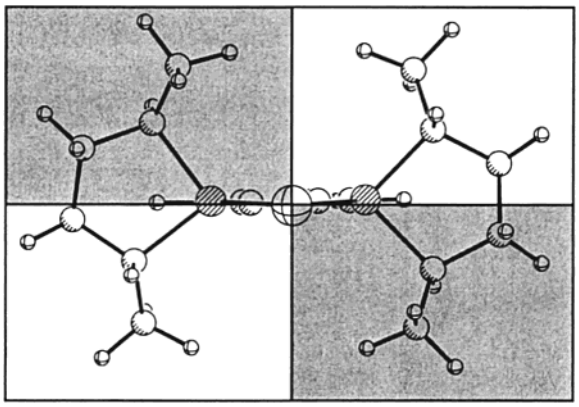

Figure 13. Representation of (*R*,*R*)-Me-DuPHOS in a quadrant diagram. Shaded quadrants indicate steric hindrance due to the methyl group projecting toward the substrate.

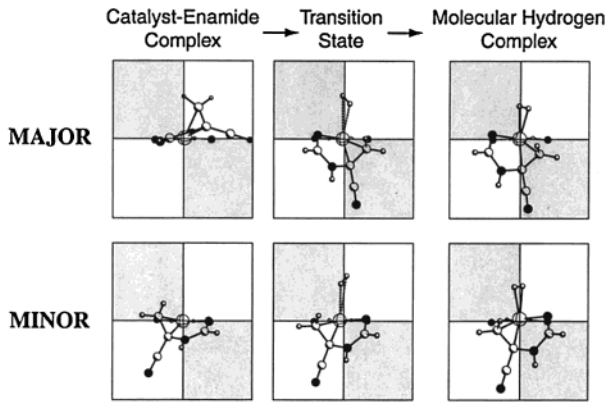

Figure 14. Addition of H_2 along pathway **A** of both manifolds. The phosphorus atoms and bridging carbons of the DuPHOS ligand are still shown. Some hydrogens have been removed for clarity.

the α- and β-substituents. These tuning effects will be the subject of a future publication.

Steric interactions between phospholane methyl groups of DuPHOS and the enamide β-carbon force the β-carbon of **MIN** to lie in the P−Rh−P coordination plane; these steric interactions originate at the β-carbon position and are significant for all substitution patterns at the β-carbon. Quadrant diagrams[3] are useful for visualizing this interaction. Figure 13 shows the DuPHOS ligand as seen from the coordination site of the enamide, and its quadrant representation. The methyl groups that project toward the enamide are depicted as shaded quadrants to indicate the steric congestion of those regions. Figure 14 shows the **MAJ** and **MIN** diastereomer structures overlaid on the quadrant diagrams. It is clear that placing the α-carbon in the P−Rh−P plane would put the β-carbon in a hindered quadrant in **MIN**, but in an unhindered quadrant in **MAJ**. As a result, steric forces in **MIN** push the α-carbon out of the P−Rh−P plane, and a substantial electronic penalty is paid. The nitrile function of **MAJ** encounters little steric interaction with a hindered quadrant because the α-carbon lies just slightly above the P−Rh−P coordination plane.

Now we turn to the reactivity difference between the diastereomers. Figure 14 depicts the formation of the molecular hydrogen complexes along pathway **A** for both manifolds. The **MIN** diastereomer needs only to distort slightly in order to accommodate the hydrogen; this motion places the enamide in the unhindered quadrant. The situation is very different for **MAJ**. The C=C double bond must move and rotate considerably, in the process losing the electronic benefit of having the α-carbon in the plane and forcing the nitrile into a hindered quadrant. This creates a large (∼20 kcal/mol) barrier to formation of the molecular hydrogen complex on major pathway **A**, with a concomitant reduction in the reactivity of the major diastereomer. In contrast, the steric and electronic effects that destabilize the **MIN** diastereomer actually assist in the association of H_2.

Quadrant diagrams suggest that addition of H_2 to **MAJ** from the opposite face (i.e., the bottom of Figure 14) should be facile. We find that this is, indeed, the case. Addition of hydrogen from the bottom leads to **DIHY-C** with very small barriers, the lowest for any dihydride. However, **DIHY-C** is in a configuration that leads to a β-alkyl hydride, which encounters a large barrier for migratory insertion. Although **DIHY-C** formation is kinetically favored, addition along this pathway is unproductive for catalysis.

Once the diastereomeric molecular hydrogen complexes (**MOLH$_2$-A** and **molh$_2$-a**) are formed along pathways (**A**,**a**), both diastereomers must cross similarly low-energy barriers for oxidative addition to form the dihydride isomers. Thus, most of the differential reactivity of the **MAJ** and **MIN** diastereomers is revealed in the relative stabilities of the molecular H_2 complexes.

B. Comparison of Computed Relative Stability and Reactivity with Empirical Data. For the most part, detailed mechanistic information on asymmetric hydrogenation exists for aryl phosphine ligands, not DuPHOS. Therefore, there is a lack of empirical data to directly compare with our computations. However, the data that do exist allow us to test some general features of our computational results, such as the difference in diastereomer stability ($\Delta\Delta G°$) and the difference in reactivity ($\Delta\Delta G^‡$, detectable as % ee). A ^{31}P NMR study by Armstrong, Brown, and Burk on the reaction of [Ir(DuPHOS)(methyl α-acetamidocinnamate)]$^+$ with H_2 established several important empirical properties.[35] First and foremost, nonequilibrium mixtures of major and minor diastereomers of [Ir(DuPHOS)(methyl α-acetamidocinnamate)]$^+$ were generated, and the higher reactivity of the minor diastereomer with H_2 was demonstrated. Similar experiments for the [Rh(DuPHOS)(methyl α-acetamidocinnamate)]$^+$ diastereomers were not possible. However, a lower limit on the equilibrium ratio of [major diastereomer]/[minor diastereomer] of 100:1 can be approximated from their failure to detect any minor diastereomer by ^{31}P NMR. Our computed $\Delta\Delta G°$ value of 3.6 kcal/mol corresponds to a 500:1 ratio of diastereomers, well over the experimental lower limit, albeit for a different enamide. In contrast, hydrogenations with aryl phosphine ligands have much smaller values of $\Delta\Delta G°$. Landis and Halpern found a $\Delta\Delta G°$ of 1.4 kcal/mol at 298 K for the [Rh(DIPAMP)(methyl (*Z*)-α-acetamidocinnamate)]$^+$ diastereomers, which allowed for NMR detection of the minor diastereomer.

The difference between the overall barrier heights along the minor and major manifolds, $\Delta\Delta G^‡$, determines the enantio-

selectivity of the reaction. We calculate a $\Delta\Delta G^{\ddagger}$ of 4.42 kcal/mol, which translates to an enantiomeric excess (ee) of 99.9% (eq 1). Experimentally, $[Rh(DuPHOS)]^+$-catalyzed hydrogenations of enamides routinely exhibit ee values of >99%. For example, the closest analogue to our model enamide that has been examined experimentally is methyl α-acetamidoacrylate; for this substrate an ee of 99.0% has been reported by Burk for the $[Rh(DuPHOS)]^+$ catalyst.[10]

$$\%\ \text{ee} = \frac{\exp(\Delta\Delta G^{\ddagger}/RT) - 1}{\exp(\Delta\Delta G^{\ddagger}/RT) + 1} \times 100\% \qquad (1)$$

C. Comparison with Other Empirical Data. Our computational study directly addresses the DuPHOS-ligated catalyst only. On the basis of the observation of an increase in reaction enantioselectivity with increasing H_2 pressure, Marinetti and co-workers[63] argue that the hydrogenation of enamides catalyzed by rhodium complexes of bis-phosphetane (CnrPHOS) diphosphines proceeds via preferred reaction of the *major diastereomer*. These authors extend this conclusion to DuPHOS catalysts on the basis of the observation that DuPHOS ligands having the same sense of chirality as CnrPHOS yield the same product chirality. Our results do not support the extension of the CnrPHOS interpretation to the DuPHOS system (for which the enantioselectivity is not significantly affected by changes in the H_2 pressure). One likely source of confusion concerns the identity of the major and minor diastereomers. The orientation that Marinetti and co-workers propose for the major diastereomer, coordination of the *si* face of the enamide to the catalyst, is our calculated *minor* diastereomer. We note that the detailed kinetics, and perhaps even the reaction mechanisms (as suggested recently by Gridnev et al.[64]), of enamide hydrogenation reactions are sensitive to the nature of the phosphine ligand.

The higher thermodynamic and kinetic stability of Ir vis-à-vis Rh cationic dihydrides provides unique insights into key thermodynamic and kinetic issues associated with oxidative addition reactions. For example, the reactions of $[Ir(diphosphine)(COD)]^+$ (COD = 1,4-cyclooctadiene) complexes with H_2 at low temperatures yield dihydrides, whereas the reactions of rhodium analogues do not.[65] When the diphosphine is chiral, two dihydride diastereomers commonly are observed. The kinetic and thermodynamic selectivities of the dihydrides are not identical. According to our stereochemical model, H_2 addition to $[Ir((R,R)\text{-Me-DuPHOS})(COD)]^+$ will occur such that movement of the COD ligand is in the same direction as the twisting of the COD ligand in the square planar ground state to yield the Λ isomer (Figure 15). Previous NMR studies reported by Landis, Kimmich, and Somsook[65] have established that the Λ-forming reaction pathway occurs ca. 50 times faster than that forming the Δ isomer at −80 °C. Thus, our simple model correctly estimates the kinetically preferred isomer formed by oxidative addition to $[Ir((R,R)\text{-Me-DuPHOS})(COD)]^+$.

A key feature of our computed mechanism is the finding that the kinetics of H_2 activation do not correlate with the thermodynamic stabilities of the dihydrides. The spectroscopic studies reported by Brown and Maddox[66] provide a rare glimpse into the dynamics of the reaction of H_2 with an Ir complex containing a coordinated, nonprochiral amido-alkene. These researchers found that addition of H_2 at −70 °C initially generates two dihydride diastereomers, each having one hydride trans to P and one hydride trans to C═C (Figure 16). These observations closely parallel our computational results, in which addition of H_2 to either **MAJ** or **MIN** occurs much more rapidly along pathways **A** and **C**, forming dihydrides with the same trans ligand arrangements. Maddox and Brown observe that the initially formed diastereomers isomerize upon warming to a possibly more stable pair of dihydrides having hydride ligands trans to P and O. Our computations indicate that the dihydrides on the **B** and **D** pathways, which have H trans to P and O, are thermodynamically more stable than the kinetically preferred dihydrides. Although we have not performed extensive computations on Ir systems, preliminary DFT computations reveal that Ir dihydride and alkyl hydride complexes with diphosphine and enamide ligands are 10−17 kcal/mol more stable than the Rh analogues.

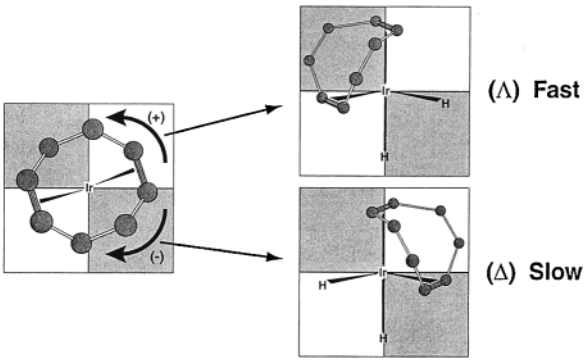

Figure 15. Approximate structure of $[Ir(bisphoshine)(COD)]^+$ on the left, showing the twist in the COD orientation.

Alkyl hydride intermediates have been observed at low temperatures (< −40 °C) during $[Rh(DIPAMP)(enamide)]^+$ hydrogenations,[23,24] but no alkyl hydrides have been observed for $[Rh(DuPHOS)(enamide)]^+$ hydrogenations. Our computations show the barriers for reductive elimination to be similar to those for oxidative addition. However, reductive elimination rates are most likely sensitive to the nature of the solvent, which may coordinate in the vacant site of the five-coordinate alkyl hydride. At this point, we can state only that our computational results are generally consistent with the observation of similar barrier heights for reductive elimination and oxidative addition, a feature that led to the interception of alkyl hydride intermediates at temperatures less than −40 °C for closely related systems.[24]

Bargon and co-workers have reported the observation of rhodium dihydride intermediates through the use of ultrasensitive para-hydrogen-induced polarization (PHIP) methods.[67] For the DuPHOS-based Rh catalysts, the steady-state concentrations extrapolated from our computations would be so small (<1 ppm of total Rh) that direct observation, even by the PHIP method, would seem to be unlikely. However, other ligand systems may give observable amounts of dihydride intermediates. Our computations also suggest the possibility that an observed dihydride could be kinetically irrelevant. For example, formation of dihydrides along the **C** pathway is thermodynamically and kinetically competitive with dihydride formation along the **a** pathway. Thus, dihydrides along the **C** pathway may be observed. However, our computational model predicts that these intermediates would not result in formation of any hydrogenated product.

(63) Marinetti, A.; Jus, S.; Genêt, J.-P. *Tetrahedron Lett.* **1999**, *40*, 8365−8368.

(64) Gridnev, I. D.; Higashi, N.; Asakura, K.; Imamoto, T. *J. Am. Chem. Soc.* **2000**, *122*, 7183−7194.

(65) Kimmich, B. F. M.; Somsook, E.; Landis, C. R. *J. Am. Chem. Soc.* **1998**, *120*, 10115−10125.

(66) Brown, J. M.; Maddox, P. J. *J. Chem. Soc., Chem. Commun.* **1987**, 1278−1280.

(67) Harthun, A.; Kadyrov, R.; Selke, R.; Bargon, J. *Angew. Chem., Int. Ed. Engl.* **1997**, *36*, 1103−1105.

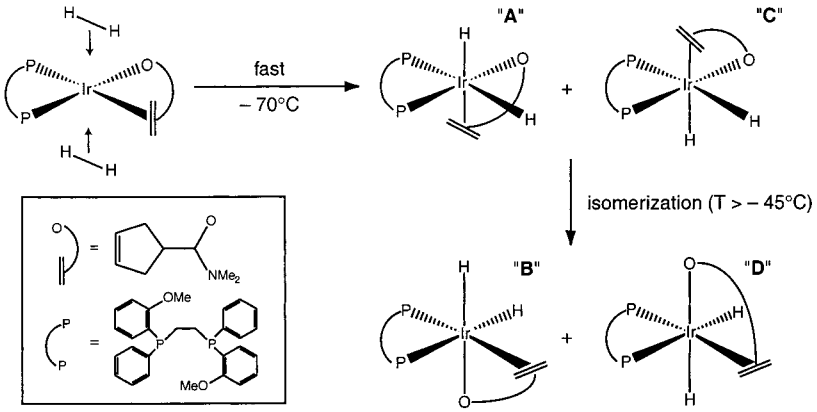

Figure 16. Dihydrides formed from addition of H_2 to an iridium amido-alkene complex. The structural labels corresponding to the dihydride intermediates in this work are given in quotation marks.

A fascinating recent result involving [Rh(DuPHOS)]$^+$ catalysts is the complete reversal of enantioselectivity reported by Burk et al. when the electron-withdrawing group on the α-carbon is replaced by a *tert*-butyl group.[68] According to our analysis, the lower stability and higher reactivity of **MIN** are due in part to the rather strong preference of the nitrile-substituted α-carbon to lie in the coordination plane of the rhodium. One might expect that this preference and, hence, the course of the reaction could be modulated by the electronic characteristics of the alkene substituents. Furthermore, one expects dramatic differences in the relative stabilities of α- and *β*-alkyl hydrides upon replacement of the small, electron-withdrawing nitrile group with the bulky, electron-donating *tert*-butyl group. We currently are performing an in-depth analysis on this problem and will report the results in a future publication.

Another interesting recent report, by Kim and Chen, concerns the gas-phase reaction of [Rh(diphosphine)]$^+$ complexes with H_2 as monitored by mass spectroscopy.[69] In principle, one could observe asymmetric hydrogenation of enamides directly by mass spectrometry. According to our computations, the prospects for such an observation are dim. If there are no intramolecular isomerization pathways between the major and minor diastereomers, as is expected for a gas-phase study, the [Rh(DuPHOS)(olefin)]$^+$ population will consist mainly of the major diastereomer. For the major diastereomer, $\Delta G^{\ddagger} = 20.37$ kcal/mol, which corresponds to a pseudo-first-order rate constant for decay of the diastereomer of 0.01 s^{-1} at 1 atm H_2. At that rate, the half-life of the reaction is about 70 s, making it unlikely a reaction would be detected in a tandem mass spectrometer operating at a far lower pressure of H_2 (ca. 1 mTorr).

VI. Summary

We have used a hybrid quantum mechanics/molecular mechanics method (ONIOM) to calculate the free energy surface for the asymmetric catalytic hydrogenation of α-formamidoacrylonitrile by [Rh((*R*,*R*)-Me-DuPHOS)]$^+$. Eight isomeric pathways along two diastereomeric reaction manifolds were investigated along a multistep reaction pathway, starting with the catalyst−substrate adduct and ending with a hydrogenated alkane coordinated to the catalyst. Of these eight pathways, four exhibit very high barriers for the formation of molecular H_2 complexes and are kinetically irrelevant. Two of the remaining pathways undergo rapid, endergonic oxidative addition but do not yield hydrogenated product due to high barriers for insertion reactions. These high barriers arise from the relative instability of the *β*-alkyl hydrides that would be formed. The less stable catalyst−substrate adduct (**MIN**) has a considerably smaller barrier for reaction with hydrogen than the more stable adduct (**MAJ**), reproducing the "anti-lock-and-key" behavior common in asymmetric hydrogenation. The identity of the carbon in the P−Rh−P plane is responsible for the difference in diastereomer stability, with the α-carbon (more substituted) exhibiting an electronic preference to be in the plane. Steric interactions force the *β*-carbon into the plane in the less stable diastereomer. The steric environment imposed by the DuPHOS ligand is also responsible for the low reactivity of the more stable diastereomer. We find that the reaction flux is carried mainly by reversible addition of hydrogen to the minor diastereomer to form a molecular hydrogen complex, followed by irreversible and turnover-limiting oxidative addition to form the dihydride and rapid insertion to form an alkyl hydride. The reductive elimination barrier is similar to the oxidative addition barrier and may become turnover limiting at low temperature. The results of the computations are consistent with all relevant empirical data.

This work demonstrates the power of quantum mechanical methods, particularly the ONIOM hybrid technique, in elucidating mechanistic details of catalytic reactions that are difficult to probe experimentally. We are continuing to explore the origins of selectivity in asymmetric hydrogenation with an emphasis on the effect of various substituents on the rate and enantioselectivity.

Acknowledgment. This work was supported by the National Science Foundation (CHE-9618497). This work was partially supported by the National Center for Supercomputer Applications under CHE970025N and utilized the computer system SGI CRAY ORIGIN2000 at the National Center for Supercomputer Applications.

Supporting Information Available: Code changes to UFF routines, sample input files, and tables of Cartesian coordinates and computed vibrational frequencies for all fully optimized intermediate and transition-state structures (PDF). This material is available free of charge via the Internet at http://pubs.acs.org.

JA0019373

(68) Burk, M. J.; Casy, G.; Johnson, N. B. *J. Org. Chem.* **1998**, *63*, 6084−6085.

(69) Kim, Y.-M.; Chen, P. *Int. J. Mass Spectrosc.* **1999**, *187*, 871−881.